ARCHIVES OF ELECTRICAL ENGINEERING VOL. 74(1), pp. 1 –19 (2025)

DOI 10.24425/aee.2025.153010

Influence of current harmonic on electromagnetic force and forced vibration in converter-fed Canned Permanent Magnet Synchronous Motors

SHUHAO ZHOU [1], MING LI [1]✉, RONG WANG [1], SHUXIAN LUN [1]

[1] *School of Control Science and Engineering, Bohai University*
No.19, Keji Road, Jinzhou, People's Republic of China
e-mail: {✉ lmpmsm,2022008028}@qymail.bhu.edu.cn

(Received: 08.08.2024, revised: 31.01.2025)

Abstract: Canned Permanent Magnet Synchronous Motors (CPMSMs) are essential components in vacuum pump systems. The stator can of CPMSMs is susceptible to deformation due to thermal stress and high-frequency harmonic electromagnetic force, leading to potential failure. When the CPMSMs are powered by an inverter power supply, it introduces time harmonic current, exacerbating the thermal stress and harmonic electromagnetic force of the system. Thus, this paper analyzes the effects of low-order current harmonics on the electromagnetic force and forced vibration of the stator can. The analytical formulation for the radial electromagnetic force of the CPMSM is obtained, taking into account the influence of harmonic current. Afterwards, the finite element model was established to investigate the space and time harmonic characteristics of the magnetic field and electromagnetic force of the stator can, and its validity was confirmed through testing on a motor test platform. Finally, modal analysis of the stator can under rated conditions and investigation of mechanical deformation induced by electromagnetic force are carried out through harmonic response analysis. This establishes a theoretical basis for improving the reliability and sealing performance of CPMSMs used in pumps.

Key words: Canned Permanent Magnet Synchronous Motor, electromagnetic force, harmonic current, stator can

1. Introduction

The Canned Permanent Magnet Synchronous Motors (CPMSMs) offer several advantages over traditional motors, including simplified maintenance procedures, enhanced cleanliness levels, and leak-proof operation [1]. The inner side of the stator must be equipped with a non-magnetic,

high-strength metal sleeve to effectively prevent vacuum leakage and serve as the driving motor for non-mechanically sealed vacuum pumps [2]. When driven by an inverter, the stator winding current of the CPMSM contains harmonic components of various orders [3], which directly impacts the performance of vacuum dry pumps, including pumping speed, ultimate vacuum, and vibration noise [4–8]. Consequently, calculating the magnetic field and forced vibration deformation of CPMSMs is crucial.

In recent decades, research on motor electromagnetic forces has primarily focused on calculation methods and control strategies aimed at mitigating their effects. Regarding the calculation of motor electromagnetic forces, numerical methods and magnetic circuit methods are commonly employed. Analytical methods mainly include the sub-domain method and magnetic potential method. J. Faiz *et al*. introduced an enhanced complex relative permeance function to consider slot effects and developed an analytical model of the air gap magnetic field influenced by static eccentricity [9]. Z. Zhihong *et al*., based on the sub-domain method, established an equivalent magnetic circuit for the generator's stator-rotor structure and gap length, calculating the distribution of the air gap magnetic field while accounting for slot effects [10]. The complex relative permeability method was employed in [11] to calculate the magnetic field of the leakage flux reverse salient-pole motor (VLF-RSPM) based on [9], while [12] utilized the magnetic field vector superposition method for comparison with literature [10]. The analytical methods, although capable of providing precise numerical values for the magnetic field in complex motor structures, are often employed during the motor design stage to evaluate motor vibration due to their computational complexity and limited applicability. In contrast, numerical methods, such as the finite element method and Maxwell tensor method, are more versatile. In [13], the finite element method was employed to compare the electromagnetic performance of linear PMSMs with different pole structures, thereby validating the effectiveness of the design method. Z. Yixuan *et al*. compared the electromagnetic forces of linear PMSMs under 3^{rd} and 7^{th} harmonic currents using the finite element method [14].

In the investigation of electromagnetic forces in CPMSMs, Y. Yali *et al*. employed analytical methods to calculate radial and tangential electromagnetic excitation forces, which were then compared with results obtained from finite element methods. This study provides a theoretical basis for mitigating vibration and noise in canned induction motors [15]. The expressions for radial electromagnetic forces under normal and eccentric conditions were derived in [16] using the tensor method. Additionally, the distribution laws of electromagnetic forces on can sleeves under different eccentric conditions were summarized. Reference [17] obtained distribution of magnetic induction intensity and electromagnetic force acting on can sleeves through harmonic analysis of electromagnetic fields inside canned motors, concluding that the electromagnetic force on the stator can is greater than that on the rotor can. Scholars have conducted extensive research on canned motors, primarily focusing on aspects such as eddy current losses, thermal effects, and structural characteristics. However, the influence of low-frequency harmonic currents, such as the fifth and seventh orders of harmonic currents introduced by the nonlinear characteristics of the inverter, on electromagnetic noise is often overlooked. The introduction of harmonic current from the inverter results in a more intricate magnetic field distribution. Given the force environment under vacuum pressure, where thermal stress on can sleeves induced by harmonic magnetic fields and eddy currents, along with electromagnetic forces, may result in local tearing, bulging, or even rupture of the can sleeves [18–20], leading to motor failure and other malfunctions, it is imperative to investigate the influence of low-frequency harmonics on the electromagnetic excitation force and forced vibration of the can sleeves.

This paper is structured as follows: Section 2 introduces and theoretically analyzes the additional harmonics generated by the inverter. It also derives the analytical formula of radial electromagnetic force for CPMSMs with harmonic current. In Section 3, it presents the details of electromagnetic modeling and simulation, analyzes the air-gap magnetic density distribution, and studies the space-time characteristics of harmonic electromagnetic forces. Section 4 includes an analysis of the mode of the stator can and an analysis of forced vibration deformation caused by harmonic current, demonstrating how additional harmonics alter vibration characteristics.

2. Electromagnetic force analysis of CPMSM fed by inverter

2.1. Harmonic current analysis

To precisely control the pressure degree during vacuum pump operation, the surface-mounted CPMSM employs flux weakening control via Space Vector Pulse Width Modulation (SVPWM). As depicted in Fig. 1, a current with a carrier frequency of 10 kHz is applied to the CPMSM stator winding. The Fast Fourier Transform (FFT) analysis of the phase current waveform is depicted in Fig. 2.

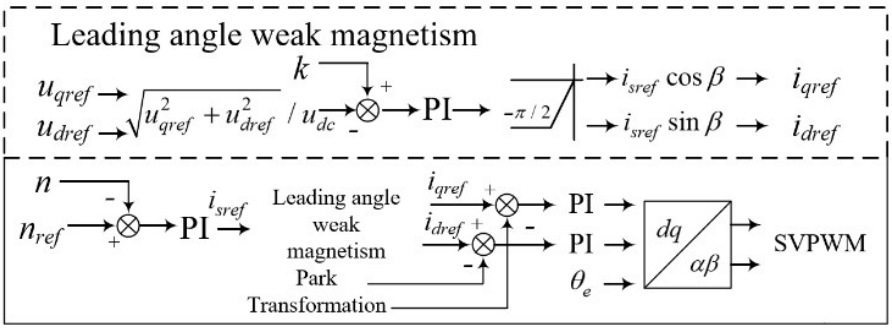

Fig. 1. SVPWM field-circuit co-simulation control block diagram

After conducting FFT decomposition on the phase current, distinct order characteristics become evident. This can be observed in Fig. 2:

1. current fundamental frequency at f;
2. low-order odd harmonic currents at frequencies of $(6k \pm 1)$ induced by inverter dead zone effects and distortion stemming from back electromotive force, such as the 5^{th}, 7^{th}, and 11^{th} harmonic currents;
3. The high-frequency sideband harmonic currents are generated by switching devices in the inverter.

The primary focus of this study is to examine the impact of 5^{th} and 7^{th} low-order odd harmonic currents on the stator can, given that high-frequency sideband harmonic currents can be easily filtered out.

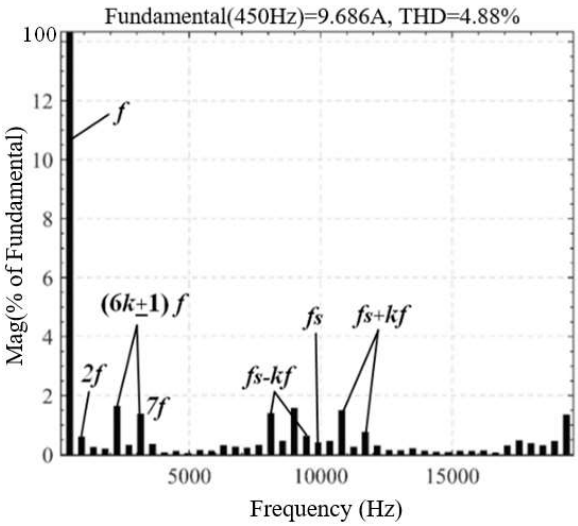

Fig. 2. FFT analysis of single-phase current

2.2. Analysis of electromagnetic exciting force of can sleeve considering harmonic current

The radial and tangential electromagnetic forces in the air gap of a CPMSM exhibit identical harmonic content, thus necessitating analysis solely on the time and space harmonic characteristics of the radial electromagnetic force. It is noteworthy that the magnitude of the radial component of magnetic flux density in the air gap of a CPMSM surpasses that of its tangential counterpart significantly. By employing the simplified Maxwell stress tensor method, we can express the electromagnetic force as [21]:

$$P_r = \frac{1}{2\mu_0}(B_r^2 - B_t^2) \approx \frac{1}{2\mu_0}B_r^2, \tag{1}$$

where: P_r is the radial electromagnetic force; B_r is the radial air gap magnetic flux density; $B_t$is the tangential air gap magnetic flux density; μ_0 is the vacuum permeability.

When supplied with sinusoidal current and considering only the fundamental wave of armature current, the motor's magnetomotive force (MMF) can be decomposed into two components: the MMF for permanent magnet excitation (as shown in Eq. 2) and the MMF for armature reaction (as shown in Eq. 3).

$$f_P(\theta t) = \sum_{u=1,3,5,\cdots} f_u \cos(up\theta - u\omega_e t), \tag{2}$$

$$f_a(\theta t) = \sum_{\infty}^{h}\sum_{\infty}^{h} f_a \cos(h\theta - \omega_e t + \phi), \tag{3}$$

where: f_u represents the amplitude of the stator's u-th space harmonic, p denotes the number of pole pairs, ω_e stands for the angular frequency of the fundamental current, t is the time, and θ indicates the phase of the magnetomotive force. Additionally, f_a signifies the amplitude of the magnetomotive force induced by the armature current, where $k = 0, \pm1, \pm2 \ldots$, and h is calculated as $(6k/d + 1)$.

The saturation effect is disregarded in the CPMSM, and the air-gap permeability harmonics primarily stem from stator slots. In the magnetic potential permeance method, the magnetic or non-magnetic properties of the stator material can indirectly alter the magnetic resistance, thereby complicating the magnetic field. When the can sleeve is composed of non-magnetic material, its circumferential reluctance is uniform and equidistant from the center of the air gap, allowing for consideration of its inner surface as an equipotential magnetic potential surface. Figure 3 illustrates the geometry of the air gap.

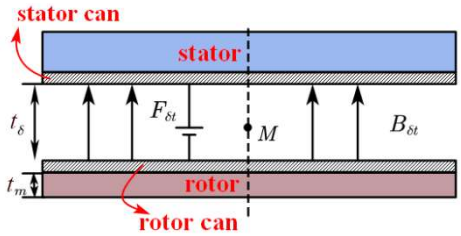

Fig. 3. Air gap structure of the CPMSM

Assuming that $B_{\delta M}$ is the magnetic density of point M and the can thickness is t_0, the magnetic potential $F_{\delta t}$ can be expressed as

$$F_{\delta t} = \frac{B_{\delta t M}(2t_0 + \delta)}{\mu_0}. \tag{4}$$

The effective air gap length of the motor can be expressed as

$$\delta = \frac{\mu_0 F_{\delta t}}{B_{\delta t}(\theta)} - 2t_0. \tag{5}$$

The air gap permeance of the CPMSM is expressed as

$$\Lambda = \frac{\mu_0}{\delta(\theta) + t_m} = \Lambda_0 + \Lambda_m \cos(mZ\theta). \tag{6}$$

In Eq. (6), Λ_0 represents the constant component of the relative magnetic flux function; Λ_m represents the amplitude of the m-th harmonic magnetic flux; Z represents the number of stator slots.

The analytical expression for the harmonic MMF produced by the armature's harmonic current is given as follows, taking into account the n-th harmonic current introduced by the inverter.

$$f_{n,h}(\theta t) = \sum_{h=(6k/d+1)p}^{\infty} \sum_{n}^{\infty} f_{n,h} \cos(h\theta - \omega_n t + \phi_{n,h}). \tag{7}$$

The expression for the radial magnetic flux density in the air gap of CPMSMs, considering additional harmonic currents in the winding and obtained using the magnetic potential method, is as follows:

$$
\begin{aligned}
B_r(\theta,t) &= \left(f_P(\theta,t) + f_a(\theta,t) + f_{n,h}(\theta,t)\right)\cdot\Lambda(\theta)\\
&= \sum_{u=1,3,5,\cdots}^{\infty} f_u\Lambda_0\cos(up\theta - u\omega_e t) + \sum_{u=1,3,5,\cdots}^{\infty}\sum_{m=1}^{\infty} f_u\,\Lambda_m\cos((up\pm mZ)\theta - u\omega_e t)\\
&+ \sum_{h=(\frac{6k}{d}+1)p}^{\infty}\frac{f_a\Lambda_0}{2}\cos(h\theta-\omega_e t+\phi) + \sum_{h=(\frac{6k}{d}+1)p}^{\infty}\sum_{m=1}^{\infty}\frac{f_a\Lambda_m}{2}\cos((h\pm mZ)\theta-\omega_e t+\phi)\\
&+ \sum_{h=(6k/d+1)p}^{\infty}\frac{f_{n,h}\Lambda_0}{2}\cos(h\theta-\omega_n t+\phi_{n,h})\\
&+ \sum_{h=(6k/d+1)p}^{\infty}\sum_{m=1}^{\infty}\frac{f_{n,h}\Lambda_m}{2}\cos((h\pm mZ_1)\theta-\omega_n t+\phi_{n,h}).
\end{aligned}
\tag{8}
$$

Substituting Eq. (8) into Eq. (1) results in the radial electromagnetic force wave of the CPMSM, taking into account harmonic currents. It's noteworthy that due to the small amplitude of the harmonic current, the magnetic flux amplitude produced by the finally two term in the Eq. (8) is also small. Thus, the electromagnetic force harmonics introduced by the harmonic current primarily interact with the fundamental magnetic field of the permanent magnet.

$$
B_p(\theta t) = B_p\cos(p\theta-\omega_e t), \tag{9}
$$

$$
f_n(\theta t) = \sum_{h=(\frac{6k}{d}+1)p}^{\infty}\sum_{m=1}^{\infty}\frac{F_{n,h}\Lambda_m B_p}{4\mu_0}\cos((h\pm mZ_1\pm p)\theta-(\omega_n\pm\omega_e)t). \tag{10}
$$

The primary space distribution and frequency attributes of electromagnetic force in CPMSMs with variable frequency drive and stator slot are outlined in Table 1.

Table 1. The number of radial electromagnetic forces affected by harmonic current

Harmonic field	**Space order**	**Frequency characteristic**
Magnetic field of permanent magnet	$(u_1 + u_2)p$	$(u_1 + u_2)\omega_e$
Armature reaction field	$(h_1 + h_2)$	$0/2\omega_e$
Magnetic field of permanent magnet + armature reaction field	$Up \pm h$	$(u+1)\omega_e$
Magnetic field of permanent magnet + slotting	$(u_1 p \pm mZ_1) \pm (u_2 p \pm mZ_2)$	$(u_1 \pm u_2)\omega_e$
Armature reaction field + slotting	$(h_1 \pm mZ_1) \pm (h_2 \pm mZ_2)$	$(1 \pm 1)\omega_e$
Magnetic field of permanent magnet + armature reaction field + slotting	$(up \pm m_1 Z_1) \pm (h \pm m_2 Z_2)$	$(u \pm 1)\omega_e$
Armature reaction field + n-th harmonic	$H \pm mZ_1$	$n\omega_e$
Magnetic field of permanent magnet +n-th harmonic	$h \pm mZ_1 \pm p$	$(n \pm 1)\omega_e$

Due to the odd symmetry of the magnetomotive force in space, where u is odd, under sinusoidal supply, the electromagnetic force only contains harmonics at frequencies that are even multiples of the fundamental frequency ω_e. If the armature winding includes 5^{th} and 7^{th} harmonic current components, given that the number of slots per pole per phase for the CPMSM is an integer, $h = (6k + 1)p$, when $k = 0$, the fundamental component of the magnetomotive force significantly surpasses the higher harmonic components. Furthermore, by neglecting the relatively minor harmonic terms of the Tooth harmonics in air-gap conductance, Eq. (10) can be simplified to:

$$f_n(\theta t) = \sum_{n}^{h=(\frac{6k}{d}+1)p} \sum_{m=0}^{\infty} \frac{F_{n,h}\Lambda_m B_p}{4\mu_0} \cos((p \pm p)\theta - (\omega_n \pm \omega_e)t). \tag{11}$$

It can be seen from Eq. (11), considering the 5^{th} and 7^{th} harmonics, the frequency and space order of electromagnetic force generated by current harmonics are as follows:

$$\begin{aligned} v &= 0, \quad f = 4f, 6f, \\ v &= 2p, \quad f = 6f, 8f. \end{aligned} \tag{12}$$

In summary, when powered by the inverter, no additional electromagnetic force harmonics are introduced. However, the radial electromagnetic force induced by inverter harmonics coincides with the inherent electromagnetic force of the motor, thereby amplifying its amplitude at that frequency. Consequently, when utilizing the inverter power supply, it is crucial to consider the impact of the motor's slot-pole ratio and the harmonics introduced by the inverter's low carrier frequency on the motor.

3. CPMSM electromagnetic field finite element analysis and experimental verification

3.1. Finite element model of CPMSM

Taking into account the pumping speed of the vacuum pump, the limit pressure, and the optional cooling system, this paper selects a 1.5 kW CPMSM as the subject of research. The essential parameters of this motor are presented in Table 2. The stator and rotor cans are fabricated from SUS316 stainless steel, which possesses high-temperature, pressure, and strong acid-alkali resistance properties. To enhance the CPMSM's high torque overload capacity while considering the impact of time harmonics on can loss, a slot-pole ratio with a low winding factor is selected for investigation in this paper. Accordingly, the motor under investigation has a slot-pole ratio of 6 poles and 9 slots. The two-dimensional finite element model of the CPMSM is illustrated in Fig. 4.

Figure 4 shows the finite element model. Some structures were simplified during the modeling process. The outer boundary of the motor was set to prevent any magnetic field from passing through, indicating no boundary leakage flux. The grid was reasonably allocated according to the magnetic pressure drop per unit distance in the magnetic circuit of the motor components. The air gap, acting as the medium for energy transfer, was meshed using a four-layer air structure. The motor air gap is 0.5 mm, with each layer being 0.125 mm, totaling 31 418 air gap grids. For the remaining

Table 2. The parameters of the CPMSM

Parameters	Value
Rated power (kW)	1.5
Phase number	3
Pole number	6
Rated frequency (Hz)	450
Can thickness (mm)	0.5
Can sleeve material	SUS316
Stator slots	9
Stator outside diameter (mm)	107
Rotor outside diameter (mm)	46
Grade of the permanent magnet	N38UH

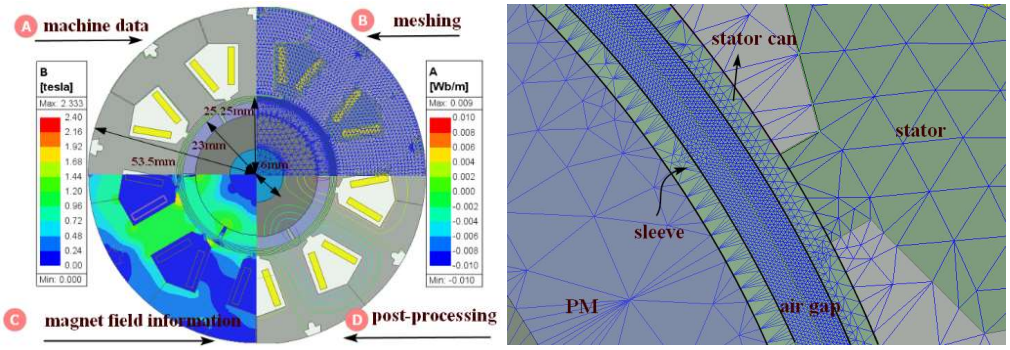

(a) (b)

Fig. 4. Finite element structure: (a) 2D finite element model of the CPMSM; (b) grid profile diagram

parts with low magnetic reluctance and low magnetic pressure drop, a double-layer meshing was used, with an internal meshing precision of 10 mm and a surface meshing precision of 0.005 mm.

In addition, before the stator unit, the groove connection method is adopted to ensure that the connection between the stator units is firm and stable, as depicted in Fig. 5(a). Under the condition of high speed, a larger centrifugal force may cause the permanent magnet to fall off and crack. Therefore, to avoid the above problems, the rotor can is installed on the outer surface of the permanent magnet. The installation of the rotor can is shown in Fig. 5(b).

Additionally, to avoid the relative motion of the magnetic steel during the operation of the CPMSM for the vacuum pump, the magnetic steel must be prevented from sustaining damage, it is necessary to ensure that the magnetic steel has optimal heat dissipation conditions, and the gap between the magnetic steel pieces needs to be filled with epoxy resin glue. The encapsulated rotor is shown in Fig. 5(c), while Fig. 5(d) depicts the rotor assembly drawing.

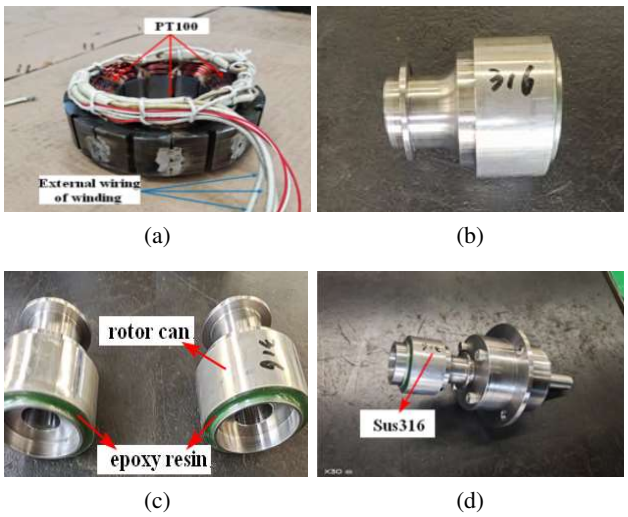

(a) (b)

(c) (d)

Fig. 5. Structure of the stator and rotor of the CPMSM: (a) prototype stator; (b) rotor can with SUS316; (c) epoxy resin filling; (d) prototype rotor

3.2. Experimental verification

To test the performance of the prototype and validate the research content of this paper, a motor test platform was built, as depicted in Fig. 6.

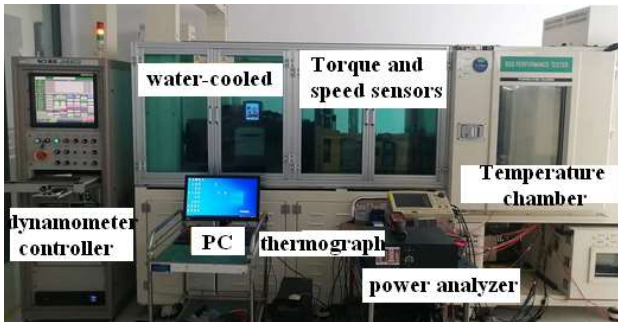

Fig. 6. Prototype test platform

The test platform comprises several components: the prototype, prototype inverter, torque and speed sensors, dynamometer, water cooling equipment and its control unit, temperature chamber, and measurement instruments such as a power analyzer, oscilloscope, temperature monitor, thermal imager, etc. The prototype frequency converter utilizes Shenzhen AD800N series high-performance vector frequency converter. The power analyzer used was Fluke's NORMA5000, and the oscilloscope employed was Yokogawa's DL750.

The back electromotive force (EMF) of prototype machines under no-load conditions was measured using the back-torque method. This entailed mechanically connecting the original motor to the machine under test and dragging the machine under test in a generator no-load operation at synchronous speed. The voltages U_{ab}, U_{bc}, and U_{ac} at the output terminals of the tested motor were measured individually, with their average values considered as the line voltage of the no-load back-EMF. The comparison between measured results and simulation results is shown in Fig. 7.

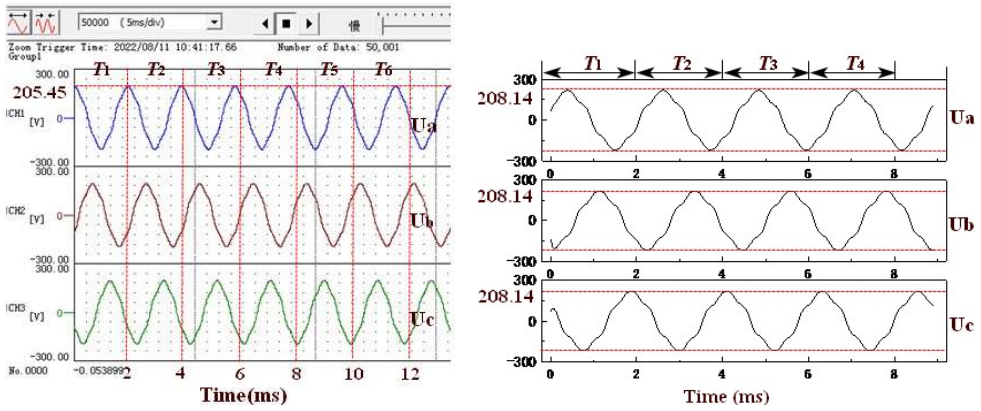

(a) (b)

Fig. 7. The waveform of EMF: (a) measured results; (b) simulation results

As shown in Fig. 7, the back-EMF waveform of the prototype is in good agreement with the simulation results. Under the rated working condition (9000 rpm/min), the CPMSM electrical period is about 2 ms. The measured no-load back electromotive force RMS of the prototype is 145.3 V, and the maximum value is 205.45 V. The simulated value of the prototype no-load back electromotive force is 147.2 V, and the maximum value is 208.14 V.

The error of the no-load back-EMF of prototypes is only 1.40%. This demonstrates the effectiveness of finite element simulation.

3.3. Electromagnetic force calculation of stator can under harmonic excitation

To investigate the magnetic field and force wave characteristics during the actual operation of the CPMSM, finite element analysis is utilized to study the magnetic field and electromagnetic force at specific locations of the can sleeve under the influence of sinusoidal current and harmonic current. Assuming the initial phase of the harmonic current is the same as that of the fundamental current. The time-space distribution of the electromagnetic force acting on the can sleeve under sinusoidal and harmonic current excitation is illustrated in Fig. 8.

In Fig. 8, the radial magnetic flux density in the air gap exhibits periodicity in its time domain, with frequency components consistent with those of the current frequency components. The effect of harmonic currents enhances the frequency components of the air gap flux density, introducing even-order harmonic components at multiples of the fundamental frequency $2f$, which are absent under sinusoidal current excitation, and augments the amplitude of low-frequency odd-order flux

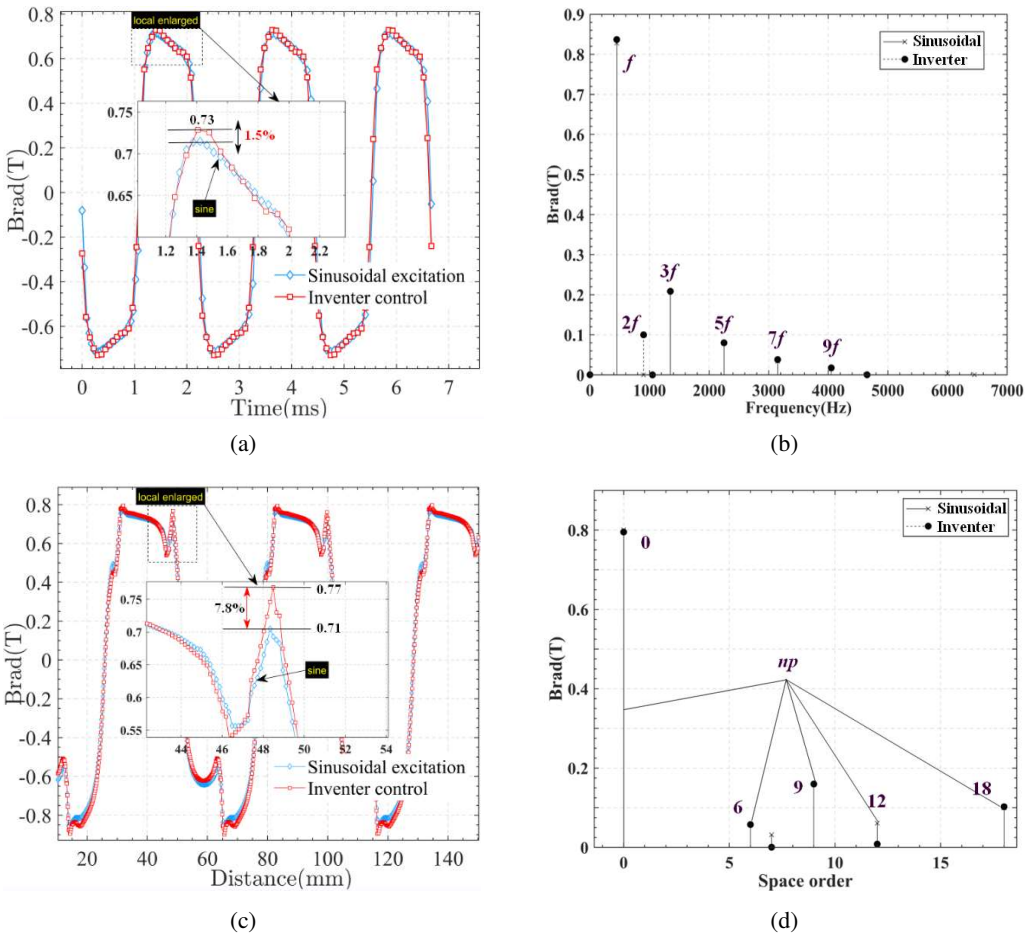

Fig. 8. The space-time distribution of the radial magnetic density: (a) time characteristics of air gap radial magnetic; (b) time characteristics FFT of air gap radial magnetic; (c) space characteristics of air gap radial magnetic; (d) space characteristics FFT of air gap radial magnetic

densities $(6k \pm 1)f$, consistent with theoretical analysis. In Figs. 8(a) and 8(c), the amplitude of air-gap magnetic density at a specific point under different excitations in one electric cycle of the canned motor is almost identical, with only a 1.5% variance. However, there is a 7.8% difference between them in terms of space characteristics at the slot. As depicted in Figs. 8(c–d), the radial magnetic flux density in the air gap of the CPMSM manifests three space cycles, corresponding to its pole logarithm. The space orders adhere to the characteristic of np, with the radial air gap magnetic flux density exhibiting a slight increase in value at its peak. The effect of harmonic currents does not augment the space order components of the air gap magnetic flux density but amplifies the amplitude of each space order.

The time-space characteristics of the radial electromagnetic force in the air gap of the CPMSM are illustrated in Figs. 9(a–b).

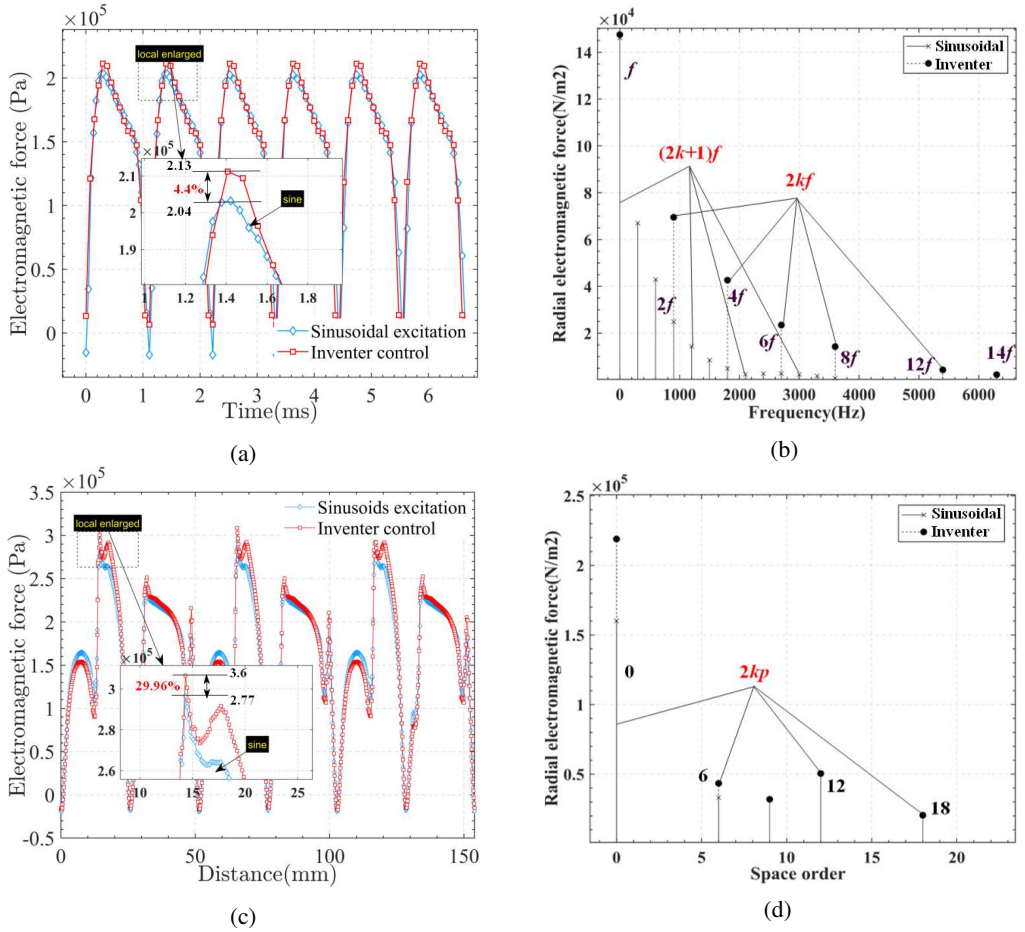

Fig. 9. The space-time distribution of the radial force density: (a) time characteristics of radial electromagnetic force; (b) time characteristics FFT of radial electromagnetic force; (c) space characteristics of radial electromagnetic force; (d) space characteristics FFT of radial electromagnetic force

The frequency components of these waves primarily comprise sinusoidal currents, low-order odd-harmonic currents interacting with the fundamental magnetic field, resulting in electromagnetic force waves with frequency characteristics of 0 and even multiples of the fundamental frequency, and harmonic currents with a frequency of $2kf$ interacting with the rotor harmonic magnetic field, resulting in harmonic waves with frequency characteristics of $(2k + 1)\ f$. As illustrated in Figs. 9(c–d), the electromagnetic force exhibit three cycles in the circumferential direction. The orders of these waves are characterized by even multiples of the pole logarithm.

In the time domain, the radial electromagnetic force under frequency converter control increases by only 4.4% compared to sinusoidal excitation, as shown in Figs. 9(a) and 9(c), due to identical time variation for both excitations. However, in terms of space characteristics, the presence of harmonic current leads to a significant increase in the amplitude of radial electromagnetic force, resulting in a difference as high as 29.96% between the two scenarios.

The magnetic flux and electromagnetic force of the motor vary over time and space position. Analyzing their changes in a specific dimension through one-dimensional FFT alone may not accurately capture their fundamental harmonic characteristics. Therefore, this paper employs time-space distribution and two-dimensional Fourier decomposition to analyze the time-space characteristics of radial electromagnetic forces under harmonic excitation, as shown in Fig. 10.

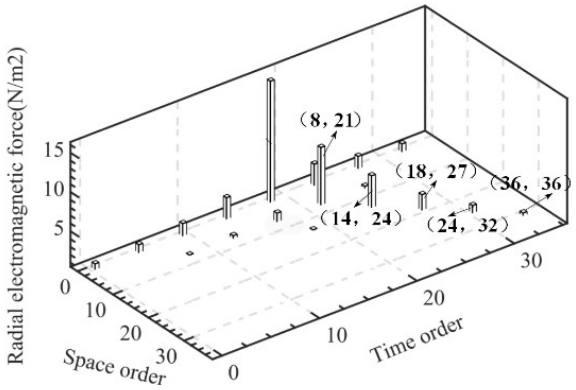

Fig. 10. The space-time distribution of two-dimensional FFT

Figure 10 reveals that the primary space orders of electromagnetic force waves in the 6 poles 9 slots CPMSM consist of multiples integers 0 and 3. Given that the amplitudes of the harmonic magnetic field and the harmonic current of the permanent magnet are substantially smaller than their respective fundamental amplitudes, the harmonic electromagnetic forces of order ($2kf$, $2kp$) resulting from the interaction of the fundamental magnetic field and the harmonic current of the permanent magnet predominantly contribute to the deformation of the can sleeve.

3.4. Electromagnetic force characteristics at key points of can sleeve

To further elucidate the characteristics of the electromagnetic force distribution in the stator can, the space distribution of electromagnetic force density at a critical point in the stator can under low-frequency harmonic excitation at rated operating conditions is depicted in Fig. 11.

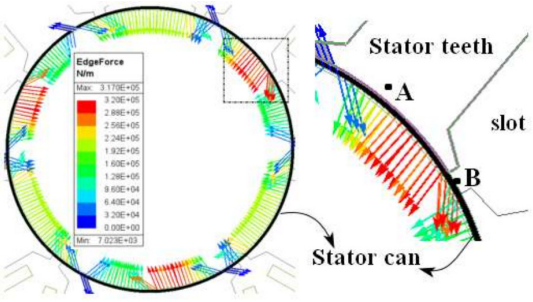

Fig. 11. Space distribution of electromagnetic force density in stator can

In Fig. 11, point A denotes a location on the can sleeve beneath the stator tooth crown, while point B is situated at the slot opening of the can sleeve. At the point B, the can sleeve undergoes both radial and tangential electromagnetic forces, alongside counteracting electromagnetic forces, which correlate with the magnetic flux distribution at the slot opening.

Conversely, at the point A, the electromagnetic force on the can sleeve primarily manifests as radial, due to the minimal tangential magnetic flux density within the stator teeth. Moreover, the electromagnetic force is notably higher at the slot opening compared to other positions on the can sleeve. Consequently, the radial electromagnetic forces resulting from eddy currents within the can sleeve, in conjunction with the harmonic magnetic field, predominantly concentrate at the slot opening. Hence, to bolster the reliability of the can sleeve, it is prudent to avoid situating axial weld seams of the can sleeve at the slot opening during installation.

4. Stator can modal analysis and forced vibration

When the radial force wave frequency of the motor is equal to or close to a certain order frequency of the can sleeve, resonance phenomena occur. The relationship between the deformation of the stator can and the order of the electromagnetic force and the structural frequency is as follows [22–24]:

$$S_v \approx \frac{F}{\left(M^2-1\right)^2\left[1-\left(\frac{f}{f_c}\right)^2\right]}, \tag{13}$$

where: S_v is the deformation amplitude of the stator can; F is the amplitude of radial electromagnetic force; M is the order of electromagnetic force; f_c is the natural frequency of the sleeve material; f is the frequency corresponding to the order of M.

From Eq. (13), it becomes evident that the deformation of the can sleeve is directly proportional to the amplitude of the radial electromagnetic force and inversely proportional to the fourth power of the electromagnetic force order. Additionally, force waves occurring more than four times exhibit minimal impact on the motor.

To study the response characteristics of the can sleeve under different loads, it is necessary to analyze the constrained modes of the can sleeve. As the ends of the stator can are welded to the end rings of the can sleeve, when performing transient dynamic and static analysis of the can sleeve, the end rings of the can sleeve should be constrained and supported to ensure consistency with the prototype. Among the various modes, the low-order modes and zero-order modes exert a greater impact on the deformation of the can sleeve. As the can sleeve has relatively minor constraints, the first-order rigid body mode can be ignored. The frequencies of the second to sixth order modes and zero-order modes are shown in Table 3.

Apart from the zero-order mode, the modal frequencies of the can sleeve increase with the order. Consequently, when the frequency of the electromagnetic force approaches the frequency of low-order modes of the can sleeve, significant vibrations occur in the can sleeve.

Table 4 presents the electromagnetic forces on the can sleeve under various harmonic currents.

Both the 5^{th} and 7^{th} harmonic currents increased the amplitude of the electromagnetic force on the can sleeve by 3.7% and 2.9%, respectively, compared to sinusoidal excitation. Since the content of the 5^{th} harmonic is higher than that of the 7^{th} harmonic, the increase in electromagnetic force

Table 3. The natural frequency of the stator can

Order	Natural frequency (Hz)
0	7033.2
2	902.64
3	1461.5
4	2234.7
5	3790.4
6	5635.4

Table 4. The electromagnetic force of the stator can

Excitation source	Radial electromagnetic force amplitude (Pa)	Tangential electromagnetic force amplitude (Pa)
Sinusoidal-excitation	292 134.83	173 555.38
5^{th} harmonic current	303 130.43	200 401.28
7^{th} harmonic current	300 561.87	190 770.47
$5 + 7^{th}$ harmonic current	326 340.29	243 884.43

amplitude due to the 7^{th} harmonic current is slightly smaller than that of the 5^{th} harmonic. When harmonic currents are coupled, the amplitude increases by 11.7%, and the greater the amplitude of the coupled harmonic, the greater its contribution to the electromagnetic force. The deformation of the can sleeve caused by electromagnetic excitation force under rated load is illustrated in Fig. 12. The maximum amplitude of the forced vibration deformation of stator can is shown in Table 5.

Table 5. The maximum amplitude value of the deformation of the stator can

Excitation source	Radial deformation (mm)	Tangential deformation (mm)
Sinusoidal-excitation	0.0115	0.0076
5^{th} harmonic current	0.0662	0.0438
7^{th} harmonic current	0.0656	0.0417
$5 + 7^{th}$ harmonic current	0.0713	0.0533

From Fig. 12 and Table 5, it is evident that in harmonic coupling, the maximum deformation of the can sleeve occurs due to the radial electromagnetic force, measured 0.07 mm per unit direction. Although the numerical value is not substantial, the displacement amplitude already represents 14% of the total thickness of the can sleeve. Subsequently, the injection of the 5th harmonic induces the next highest deformation, at 0.067 mm, accounting for 13.4% of the total thickness of the can sleeve. The deformations resulting from tangential electromagnetic forces are 8.74%, 8.3%, and 10.64% of the can sleeve thickness, respectively.

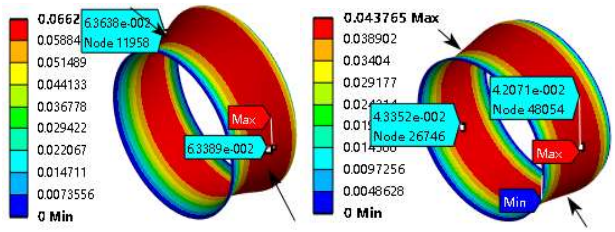

(a)

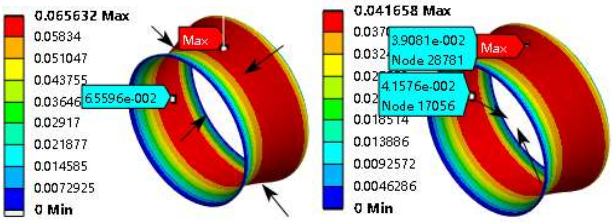

(b)

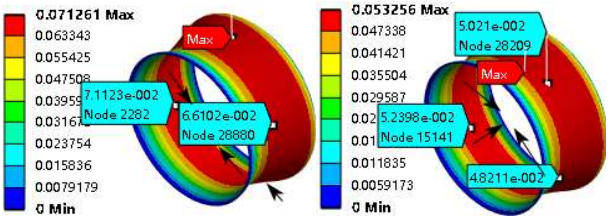

(c)

Fig. 12. The stator can amount of deformation: (a) 5th harmonic injection stator can deformation; (b) 7th harmonic injection stator can deformation; (c) 5 + 7th harmonic injection stator can deformation

Therefore, when designing CPMSMs, it is crucial to carefully consider the impact of low-order harmonic current introduced by the inverter power supply and the electromagnetic force generated by the motor itself on can sleeve deformation. Additionally, it is essential to incorporate "frequency avoidance control" into the inverter design, aiming to avoid high-frequency carrier frequencies and natural frequencies of the can sleeve material. Building upon this research, further investigation will be conducted on magnetic and amorphous alloy materials.

5. Conclusions

The current study examines the characteristics of low-order harmonic electromagnetic forces on the stator can under variable frequency driving conditions, as well as the resulting vibration-induced deformation, with validation using the finite element method. The subsequent conclusions are as follows:

1. The interaction between the fundamental magnetic field of the permanent magnet and the harmonic currents gives rise to the ($2kf$, $2kp$) harmonic electromagnetic forces, which primarily cause the deformation of the can sleeve.
2. At the slot opening of the stator, the electromagnetic force acting on the stator can includes both radial and tangential components, whereas at the tooth top position, it consists solely of the radial component. Therefore, when installing the can sleeve, it is advisable to avoid positioning the weld seam of the can sleeve at the slot opening.
3. Low-order harmonics predominantly contribute to the forced deformation of the CPMSM stator can, with the greatest displacement occurring when harmonics are coupled. The displacement of the can sleeve is maximized when coupled with the harmonic, and this displacement is directly correlated to the amplitude of the harmonic. Therefore, during the motor design phase, it is crucial to consider the impact of $(6k \pm 1)f$ low-frequency odd-order harmonics on the electromagnetic force.

Acknowledgements

This work was supported by the Provincial Education Department Project of Liaoning in China under grant no. 2021LJKZ/1020.

References

[1] Li X., Yang H., Ge J., Zhu S., Zhu Z., *Intelligent cavitation recognition of a canned motor pump based on a CEEMDAN-KPCA and PSO-SVM method*, IEEE Sensors Journal, vol. 24, no. 4, pp. 5324–5334 (2024), DOI: 10.1109/JSEN.2023.3347248.

[2] Li M., Lun S., Mu H., Wang W., *A novel temperature calculation method of canned permanent magnet synchronous motor for vacuum pump*, Archives of Electrical Engineering, vol. 73, no. 1, pp. 87–104 (2024), DOI: 10.24425/aee.2024.148859.

[3] Qiu H., Zhang Y., Yang C., Yi R., *Performance analysis and comparison of PMSM with concentrated winding and distributed winding*, Archives of Electrical Engineering, vol. 69, no. 2, pp. 303–317 (2020), DOI: 10.24425/aee.2020.133027.

[4] Qiu H., Zhang Y., Yang C., Yi R., *Influence of the number of turns on the performance of permanent magnet synchronous motor*, Archives of Electrical Engineering, vol. 68, no. 3, pp. 429–436 (2020), DOI: 10.24425/bpasts.2020.133375.

[5] Li J., Zhou F., Zhang Y., Zhang D., Liu C., Kang J., Pan S., *Effect of working fluid temperature on energy dissipation characteristics of liquid ring vacuum pump*, Applied Thermal Engineering, vol. 236, 117612 (2024), DOI: 10.1016/j.applthermaleng.2023.121469.

[6] Pan S., Wang J., Zhao X., Ren C., Xin Y., Wang Z., *New design and transient flow analysis of a claw vacuum pump with novel rotors*, Vacuum, vol. 216, 113309 (2023), DOI: 10.1016/j.vacuum.2023.112470.

[7] Kanyolo T.N., Oyando H.C., Chang C.K., *Acceleration Analysis of Canned Motors for SMR Coolant Pumps*, Energies, vol. 16, no. 15, 5623 (2023), DOI: 10.3390/en16155733.

[8] Huang Y., Jiang L., Ni Y., Lei H., Gao G., *Control method analysis with high performance and stability for permanent magnet motor based on canned structure*, International Journal of Electrical Power and Energy Systems, vol. 143, 106291 (2022), DOI: 10.1016/j.ijepes.2022.108441.

[9] Faiz J., Hassanzadeh M., Kiyoumarsi A., *Analytical calculation of magnetic field in surface-mounted permanent-magnet machines with air-gap eccentricity*, COMPEL-The International Journal for Computation and Mathematics in Electrical and Electronic Engineering, vol. 38, no. 2, pp. 893–914 (2019), DOI: 10.1108/compel-07-2018-0284.

[10] Zhihong Z., Qinkai H., Xueping X., *Air gap magnetic field calculation of permanent magnet direct drive generator based on conformal mapping and magnetic equivalent circuit method*, Transactions of China Electrotechnical Society, vol. 38, no. 3, pp. 703–711 (2023), DOI: 10.19595/j.cnki.1000-6753.tces.210769.

[11] Liu X., Zhu S., Liu D., Liang J., *Design and analysis of wide speed regulation of variable leakage flux reverse salient-pole motor*, CES Transactions on Electrical Machines and Systems, vol. 7, no. 3, pp. 284–293 (2023), DOI: 10.30941/CESTEMS.2023.00031.

[12] Ma C., Li Q., Lu H., Liu Y., Gao H., *Analytical model for armature reaction of outer rotor brushless permanent magnet DC motor*, IET Electric Power Applications, vol. 12, no. 5, pp. 651–657 (2018), DOI: 10.1049/iet-epa.2017.0751.

[13] Liu X., Gao J., Huang S., Lu K., *Magnetic field and thrust analysis of the U-channel air-core permanent magnet linear synchronous motor*, IEEE Transactions on Magnetics, vol. 53, no. 6, pp. 1–4 (2017), DOI: 10.1109/tmag.2017.2655082.

[14] Zhang Y., Zhang X., Wang Y., Zhang W., Liu J., Xu Q., *Electromagnetic force ripple suppression strategy of the micro permanent magnet linear motor*, Energy Reports, vol. 9, no. S10, pp. 1060–1072 (2023), DOI: 10.1016/j.egyr.2023.05.126.

[15] Zhu Y., Bai F., Sun J., *Multi-objective optimization algorithm for optimizing NVH performance of electric vehicle permanent magnet synchronous motors*, Journal of Power Electronics, vol. 22, no. 12, pp. 2039–2047 (2022), DOI: 10.1007/s43236-022-00519-6.

[16] Wu Q., Li W., Li J., Feng G., Zhang B., *Research on electromagnetic and structural characteristics of canned electric actuated valve permanent magnet synchronous motor under eccentricity*, IEEE Transactions on Electrical and Electronic Engineering, vol. 17, no. 8, pp. 1176–1197 (2022), DOI: 10.1002/tee.23609.

[17] Feng Y., Zhang Ji., *Simulation analysis of electromagnetic force of shielding sleeve of canned motor*, Machinery Design & Manufacture, vol. 4, no. 4, pp. 26–28 (2019), DOI: 10.19356/j.cnki.1001-3997.2012.04.010.

[18] Li M., An Y., Zhang Z., Deng W., Wang G., Qi L., Zhu S., *Effect of time harmonic current considering load condition on performance of canned induction motor*, International Journal of Applied Electromagnetics and Mechanics, vol. 66, no. 3, pp. 369–385 (2021), DOI: 10.3233/JAE-201552.

[19] Li M., An Y., Hou Q., An H., *A Novel Method for Obtaining can Loss of Canned Permanent Magnet Synchronous Motor Under Non-sinusoidal Excitation*, Journal of Electrical Engineering & Technology, vol. 19, no. 1, pp. 475–483 (2024), DOI: 10.1007/s42835-023-01562-4.

[20] Jin F., Li N., Tao R., *Investigation of the self-balance impeller of a canned motor pump for axial force reduction*, Proceedings of the Institution of Mechanical Engineers, Part C: Journal of Mechanical Engineering Science, vol. 6, no. 8, pp. 1806–1817 (2023), DOI: 10.1177/09544062221133735.

[21] Wang Y., Gao H., Wang H., Ma W., *NVH optimization analysis of permanent magnet synchronous motor by rotor slotting*, Vehicles, vol. 2, no. 2, pp. 287–302 (2020), DOI: 10.3390/vehicles2020016.

[22] Wang L., Wang X., Li N., Li T., *Modelling and analysis of electromagnetic force, vibration, and noise in permanent magnet synchronous motor for electric vehicles under different working conditions considering current harmonics*, IET Electric Power Applications, vol. 17, no. 7, pp. 952–964 (2023), DOI: 10.1049/elp2.12315.

[23] Verez G., Barakat G., Amara Y., Hoblos G., *Impact of Pole and Slot Combination on Vibrations and Noise of Electromagnetic Origins in Permanent Magnet Synchronous Motors*, IEEE Transactions on Magnetics, vol. 51, no. 3, pp. 1–4 (2015), DOI: 10.1109/tmag.2014.2354019.

[24] Valavi M., Nysveen A., Nilssen R., Lorenz R.D., Rølvåg T., *Influence of Pole and Slot Combinations on Magnetic Forces and Vibration in Low-Speed PM Wind Generators*, IEEE Transactions on Magnetics, vol. 50, no. 5, pp. 1–11 (2014), DOI: 10.1109/tmag.2013.2293124.